

Pressure Dependence of Electrical Conductivity of Black Titania Hydrogenated at Different Temperatures

Junxiu Liu,[†] Jiejuan Yan,[†] Qiwu Shi,^{‡,§} Hongliang Dong,[†] Jinbo Zhang,^{†,§} Zhongwu Wang,^{||} Wanxia Huang,[‡] Bin Chen,[†] and Hengzhong Zhang^{*,†,§}

[†]Center for High Pressure Science and Technology Advanced Research, Shanghai 201203, China

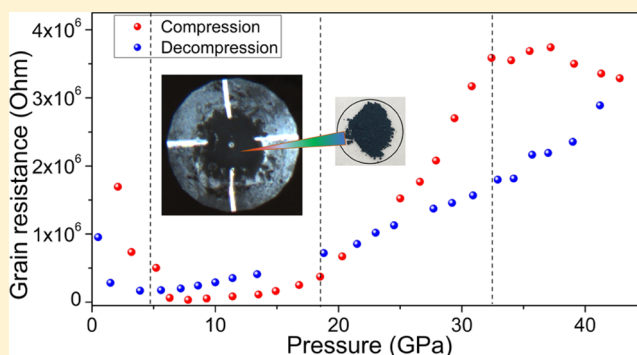
[‡]College of Materials Science and Engineering, Sichuan University, Chengdu, Sichuan 610064, China

[§]College of Physical Science and Technology, Yangzhou University, Yangzhou, Jiangsu 225002, China

^{||}Cornell High Energy Synchrotron Source, Cornell University, Ithaca, New York 14853, United States

Supporting Information

ABSTRACT: Temperature can control the degree of hydrogenation of titania (i.e., black TiO₂), determining the defect chemistry and hence its optical absorption and electrical conductivity that are key to the photocatalytic activity. However, how pressure affects the two key factors is unknown. In this work, we used a diamond anvil cell to produce the required high pressure (HP) and studied the pressure dependences of the structure change, the electrical conductivity, and the light absorption of black titania using HP X-ray diffraction, Raman/UV–vis spectroscopy, and electrical transport measurements. Results reveal that accompanying the HP phase transition the electrical conductivity exhibits complex variation with pressure, in good accord with the band gap changes of involved HP phases as a function of pressure. This confirms the assumption that pressure affects the electrical conductivity of black titania via controlling the number of free electrons (holes) distributed in the conduction (valence) band, which is inversely proportional to the exponent of the band gap that scales almost linearly with the pressure. This work provides a fundamental understanding of the pressure-induced structure–property relationship in black titania and will have important implications for tuning the photocatalytic activity via pressure and for developing new applications such as pressure sensors.



This confirms the assumption that pressure affects the electrical conductivity of black titania via controlling the number of free electrons (holes) distributed in the conduction (valence) band, which is inversely proportional to the exponent of the band gap that scales almost linearly with the pressure. This work provides a fundamental understanding of the pressure-induced structure–property relationship in black titania and will have important implications for tuning the photocatalytic activity via pressure and for developing new applications such as pressure sensors.

1. INTRODUCTION

As an important semiconductor material, titania (TiO₂) has been studied extensively because of its wide applications in photocatalysis,^{1,2} gas sensors,³ and energy conversion and storage.^{4,5} For these applications, it is required that TiO₂ exhibits outstanding functions in light absorption, electron–hole separation, and electron transport. However, major TiO₂ phases have wide electronic band gaps (3.0–3.4 eV)^{6–8} and low electrical conductivity, resulting in relatively low solar energy utilization and/or quantum yield. Efforts have been made to improve its functions through introduction of impurities and/or defects in the TiO₂ lattice. Metal and nonmetal doping can generate impurity energy levels between the valence and conduction bands of TiO₂, forming mid-gap states that facilitate solar absorption and improve the photocatalytic activity.^{8–12} Moreover, it was found that defect introduction by hydrogenation (partial reduction of TiO₂ by hydrogen) is very effective in shifting its band gap to around 1.5 eV, producing significant enhancement in light absorption.¹³ Due to the strong light absorption, hydrogenated TiO₂ appears dark in color and hence is often called black titania.

Now, it is well established that black titania has a hydrogen-stabilized amorphous layer surrounding a crystalline core, forming an amorphous shell/crystalline core structure that possesses high capability of solar light absorption, increased photocatalytic activity, and better electrical conductivity due to the existence of abundant oxygen vacancies, some Ti³⁺ cations, and the amorphous shell.^{6,14–16} Narrowing of the band gap and enhancement of the electrical conductivity are important to increasing the photocatalytic activity of titania as the former can improve the optical absorption and the latter can facilitate the electron–hole separation.¹⁷ Moreover, first-principles calculations unveiled different oxidative and reductive capabilities of different facets of anatase crystals.¹⁸ This may also be applicable to hydrogenated black titania, predicting morphology-dependent photocatalytic activities.

In addition to structure modification using doping and defects at ambient conditions, pressure as a fundamental state

Received: December 14, 2018

Revised: January 19, 2019

Published: January 28, 2019

variable provides a clean way to adjust the crystal and electronic structures of materials and hence affects the physical and chemical properties of materials. At ambient pressure, TiO₂ has four natural polymorphs: rutile, anatase, brookite, and columbite (α -PbO₂-type, i.e., TiO₂-II) phases.^{19–21} Among these, rutile is the most thermodynamically stable one.²² Under compression, pressure induces phase transition of bulk rutile TiO₂ to the baddeleyite phase of TiO₂ at \sim 12 GPa,^{23–25} while in \sim 30 nm nanocrystals, baddeleyite phase starts to form at \sim 8 GPa.²⁶ Pressure-induced amorphization in bulk and nanocrystal TiO₂ was also observed at \sim 16.4 GPa.²⁶ The high-pressure (HP) baddeleyite phase commonly transforms to the TiO₂-II phase upon decompression.^{23,26} However, so far, it is unknown which HP phase transitions can occur in black titania and how pressure affects its electrical conductivity. In particular, the structure–electrical conductivity relationship at high pressure and the underlying mechanism are yet to be explored. The obtained knowledge will be useful for evaluating the application of pressure for modulating the electrical conductivity and hence the photocatalytic activity of TiO₂ on top of the defect effect introduced by hydrogenation. Thus, in this work, we determined the pressure dependence of the structure change of black titania using HP X-ray diffraction (XRD) and Raman spectroscopy and measured the light absorption and electrical conductivity using UV–vis spectroscopy and electrical transport measurements at high pressure. From combined experimental data and density functional theory (DFT) calculations, the mechanism accounting for the pressure dependence of the electrical conductivity was elucidated. The knowledge generated from this work may be transferable to other oxide systems and should be useful for developing new applications of hydrogenated TiO₂ such as pressure and light sensors.

2. EXPERIMENTAL DETAILS

2.1. Synthesis and Characterization. Black titania samples were prepared through hydrogen reduction of rutile particles at four temperatures (500, 600, 700, and 800 °C): the precursor rutile TiO₂ powders were heated at a speed of 10 °C/min to the set temperature and annealed for 1 h, followed by slow cooling to room temperature. The whole process was carried out in pure hydrogen gas at a flow rate of around 1.0 L/min.

XRD was used to determine the crystal structure of the prepared samples using an X-ray diffractometer (Malvern Panalytical) with Cu K α radiation (wavelength 1.54056 Å). XRD patterns were collected over a range of 2θ from 10 to 90° at a scanning rate of 5°/min. Particle morphology and particle sizes of the samples were observed using a transmission electron microscope (TEM) operated under 200 keV (Tecnai G2 F20 S-TWIN, FEI). A TEM specimen was prepared by dripping a drop of dilute TiO₂ ethanol suspension (formed under ultrasonic agitation) onto a copper TEM grid. UV–vis absorption measurements of the samples were carried out using an Agilent Cary 5000 double-beam, double-monochromator spectrophotometer. The spectra of TiO₂ samples were recorded in the wavelength range of 200–800 nm with a poly(tetrafluoroethylene) integrating sphere attachment.

In this work, we had chosen two black titania samples (that hydrogenated at 500 and 800 °C) for high-pressure experimental studies (below).

2.2. In Situ High-Pressure XRD and Raman Spectroscopy. A diamond anvil cell (DAC) was used to generate

required high pressures. The culet size of the anvils is 300 μ m in diameter. A stainless steel gasket was preindented to 28 μ m in thickness, and then a hole of 150 μ m in diameter was drilled through the center of the indentation using laser-drilling, acting as the sample chamber. A tiny amount of finely ground black titania powders was loaded into the DAC together with a few grains of ruby as the pressure calibrant. A methanol/ethanol mixture (4:1) was used as the pressure transmitting medium for the XRD and Raman spectroscopy measurements. In situ high-pressure XRD measurements were performed at the B1 beamline station of the Cornell High Energy Synchrotron Source. XRD patterns were collected using a Mar345 image plate detector at a monochromatic X-ray wavelength of 0.4859 Å.²⁷ The sample-to-detector distance was calibrated using a CeO₂ standard. The diffraction images were integrated using the Fit2d program²⁸ to yield numerical intensity versus 2θ data. Rietveld analyses were performed on chosen XRD data using GSAS software to identify and/or verify the phases present and to refine their crystal structures as well.²⁹ High-pressure Raman data were collected using a Raman spectrometer (inVia Reflex, Renishaw) with a 532 nm excitation laser.

2.3. In Situ High-Pressure Electrical Transport Measurements. High-pressure electrical transport measurements of samples were performed in situ while a sample was under compression in a DAC. For loading a sample into the DAC, a T301 stainless steel gasket was preindented to 30 μ m in thickness and a hole of 250 μ m in diameter was drilled through the gasket center. A thin layer of cubic boron nitride (cBN) was pressed onto the gasket for insulating electrodes from the gasket. A hole with a diameter of 130 μ m was then drilled through the cBN center for loading a powder sample into the DAC. Pressures of the sample were determined using the ruby luminescence method. No pressure transmitting medium was used to ensure good electrical contact of the electrodes with the sample and to prevent possible introduction of impurities and electrode short circuit as well. Electrical transport measurements were conducted using an alternating current (ac) impedance method and/or a direct current (dc) van der Pauw method.³⁰ With the first one, two electrodes were attached to the sample contained in the DAC and the ac impedance spectra were measured using a CS353 impedance analyzer (Wuhan CorrTest Instruments Corp., Ltd.) in the frequency range of 0.01 Hz to 10 MHz. The measurements yielded electrical resistance (in the unit of ohm) of a sample after data modeling. With the second one, four probing electrodes were attached to the sample contained in the DAC and two electrical resistances from two pairs of the electrodes were determined using a Keithley 6221 dc/ac source and a Keithley 2182A nanovoltmeter, which were utilized to provide the direct current and probe the voltage drop, respectively. The electrical resistivity (in the unit of $\Omega\cdot$ m) of the sample could be derived by fitting the data to the basic equation of the van der Pauw method (see below).

2.4. In Situ High-Pressure UV–Vis Absorption Spectroscopy. For high-pressure UV–vis absorption measurements, a pair of diamonds that yield very low fluorescence under laser illumination (which are typically for high-pressure infrared measurements) were used in the DAC set. Silicon oil was used as the pressure transmitting medium. The UV–vis absorption spectra of the black titania samples were collected using a UV–vis absorption spectrophotometer (a custom-built system) with a response time of 1 s in the wavelength range

from 200 to 800 nm. From data analyses of the spectral data, band gaps of the black titania samples can be deduced (see below).

3. COMPUTATIONAL DETAILS

The electron densities of states (DOSs) of several TiO_2 phases (anatase, rutile, baddeleyite, $\text{TiO}_2\text{-II}$, and $\text{TiO}_2\text{-OI}$) and a Magneli phase Ti_9O_{17} at different pressures were calculated using the density functional theory (DFT) implemented in the Quantum Espresso (QE) package.³¹ The computations were conducted using an integrated graphic user interface and running environment of QE, Burai (v.1.3.2).³² The projector augmented-wave (PAW) pseudopotential functions³³ of Ti and O with energy cutoff of ~ 52 Ry and charge density cutoff of ~ 575 Rd and Perdew–Burke–Ernzerhof exchange correlations³⁴ at the GGA + U approximation³⁵ were used for the calculations, where the Hubbard correction parameter U was taken as 6.0 eV for both Ti and O atoms.³⁶ At a given pressure, the crystal structure of a Ti–O phase was optimized first. Then, the DOS of the optimized structure was calculated. The band gaps of the concerned Ti–O phases at different pressures were estimated from the DOS diagrams.

4. RESULTS AND DISCUSSION

4.1. Sample Characterization. The color of the TiO_2 samples changed from initially white (untreated) to increasingly darker as the reduction temperature increased from 500 to 800 °C (Figure 1a), indicating different defect states in TiO_2 particles owing to the presence of oxygen vacancies and particle surface disorder.^{37–39} TEM images (Figure 1b) reveal that the TiO_2 crystals are nanorods or fatty nanoparticles ~ 60 nm in diameter.

The structures of the TiO_2 samples were identified using XRD (Figure 1c). The pristine TiO_2 is in the rutile phase with a tetragonal ($P4_2/mnm$) structure. The samples hydrogenated at 500, 600, and 700 °C can all be indexed as the rutile phase, whereas those hydrogenated at 800 °C can be identified as a mixture of rutile and Magneli phases, Ti_9O_{17} , in a triclinic ($P\bar{1}$) structure (ICSD #35124⁴⁰). The Magneli phase is a derivative phase of rutile featuring a crystallographic shear structure in which dense planar defects are regularly introduced into the mother rutile structure.^{41–43} At 800 °C, faster hydrogen reduction deprived the rutile phase of more oxygen, causing more oxygen deficiencies and hence partial formation of the Magneli phase.

The UV absorptions (in the wavelength range $\lambda = 200\text{--}400$ nm; Figure 1d) of the TiO_2 samples are determined by the intrinsic band gap of the rutile phase (~ 3.0 eV). The similarity of their UV spectra suggests that oxygen vacancies at the particle surfaces have trivial effects on UV absorption. However, a TiO_2 sample hydrogenated at a higher temperature exhibits larger absorption in the visible to the near-infrared light region ($\lambda > 400$ nm; Figure 1d). This can be attributed to the creation of mid-gaps between the valence band and conduction band in the sample after hydrogenation.^{13,38} The higher the temperature, the more the surface defects and the more the mid-gap energy levels and hence the more visible light absorption. This is consistent with the observation (Figure 1c) that the sample hydrogenated at 800 °C had even formed the defect-rich Magneli phase Ti_9O_{17} .

4.2. Phase Transition at High Pressure. High-pressure XRD patterns of TiO_2 hydrogenated at 500 and 800 °C are

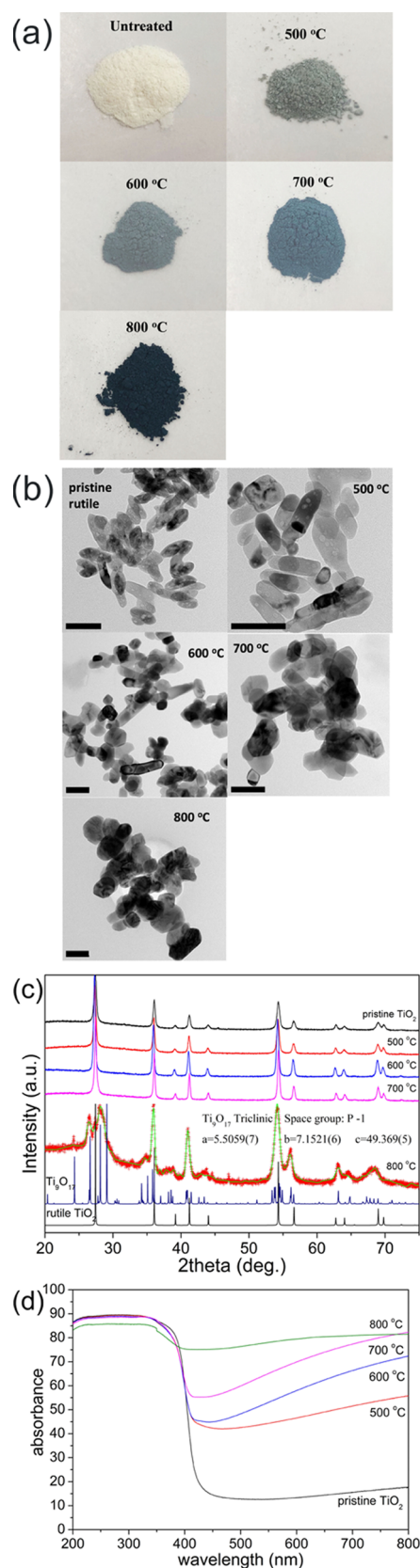


Figure 1. (a) Photos, (b) TEM images, (c) XRD patterns, and (d) UV–vis absorption (in percentage scale) spectra of untreated pristine TiO_2 and black titania nanocrystals hydrogenated at 500, 600, 700, and 800 °C. In (b), scale bar = 100 nm; in (c), X-ray wavelength is 1.54056 Å and the bottom two curves are calculated patterns of rutile and Ti_9O_{17} for reference.

shown in Figure 2. For TiO_2 hydrogenated at 500 °C, beginning at ~ 17.0 GPa, the (111) peak of the baddeleyite phase (space group $P2_1/c$; also denoted the MI phase) appeared at $\sim 10.7^\circ$. At 18.8 GPa, obvious phase transition from rutile to baddeleyite was observed and the rutile phase was still present until ~ 25.7 GPa. On further compression above 27.0 GPa, the material started to transform to the orthorhombic TiO_2 -OI phase with a space group of $Pbca$ (Figure 2b) and the baddeleyite phase and the OI phase coexisted up to the highest experimental pressure of 34.2 GPa, as confirmed by Rietveld fittings shown in Figure 2b. This coexistence may arise from the similarity in their structures.^{44–47} On decompression to below ~ 3.0 GPa, the mixture of TiO_2 -OI and baddeleyite transformed to the TiO_2 -II phase.

According to previous studies,^{44,48–51} at ambient temperature, the expected sequence of phase transformation of TiO_2 is rutile \rightarrow TiO_2 -II \rightarrow MI \rightarrow OI \rightarrow OII. Many experiments confirmed the rutile \rightarrow MI transition below 60 GPa.^{24,52,53} Previous theoretical calculations predicted the presence of the OI phase from 50 to 70 GPa,⁵¹ whereas experiments showed its existence after laser heating of TiO_2 at 1300–1500 K and at a pressure from 28 to 32 GPa.⁵¹ Differing from this, our present work revealed that the TiO_2 -OI phase can form at ambient temperature at only ~ 27 GPa, far below the predicted 50–70 GPa. Recent DFT and phonon calculations by Mei et al. showed that at 300 K the MI and OI phases become stable at $> \sim 12$ GPa and ~ 20 GPa, respectively.⁵⁴ Our experiment result is closer to the recent calculation results⁵⁴ than to previous ones.⁵¹ We infer that in hydrogenated titania, defects may serve as nucleation centers of new phases, which can lower the kinetic barrier for transformation of black TiO_2 and hence the OI phase could form at ambient temperature rather than at very high temperature as in ref 51.

In the XRD patterns of the sample hydrogenated at 800 °C (Figure 2c), some baddeleyite peaks (marked “MI”) and some unknown peaks (marked “*”) appeared at 22.9 GPa. It is possible that the Magneli phase Ti_9O_{17} present had transformed to an unknown high-pressure phase accompanying (or even prior to) the phase transition of rutile to the baddeleyite phase. The MI phase and the unknown phase coexisted to the highest pressure of 44.4 GPa. In decompression, the MI phase transformed to the TiO_2 -II phase as the pressure decreased to < 2.3 GPa, as verified by Rietveld fitting (Figure 2d). The triclinic Ti_9O_{17} phase and its possible high-pressure phase were not observed after decompression, possibly due to their oxidation and conversion to the TiO_2 -OI phase while in decompression (Figure 2d).

High-pressure Raman data were collected for further confirming the XRD-derived phase transitions (Figure S1; Supporting Information). Three main peaks attributed to the Raman modes of the multiphoton process (~ 220 – 240 cm^{-1}), E_g (~ 430 – 450 cm^{-1} at 0.9 GPa), and A_{1g} (~ 600 – 610 cm^{-1} at 0.9 GPa) can be observed in many spectra of the two samples in compression (Figure S1a,c). In the Raman spectra of TiO_2 hydrogenated at 500 °C (Figure S1a), at 21.1 GPa and above, all of the Raman peaks centered at around 206, 237, 267, 281, 323, 385, 435, 448, 502, 714, and 752 cm^{-1} belong to the MI phase. This indicates the phase transition from rutile to baddeleyite at above 21.1 GPa. Beginning at 32.3 GPa, some Raman peaks disappeared and several new peaks appeared, with the latter corresponding to the formation of the TiO_2 -OI phase. However, in the Raman spectra of the TiO_2 hydrogenated 800 °C (Figure S1c), there are no obvious peaks

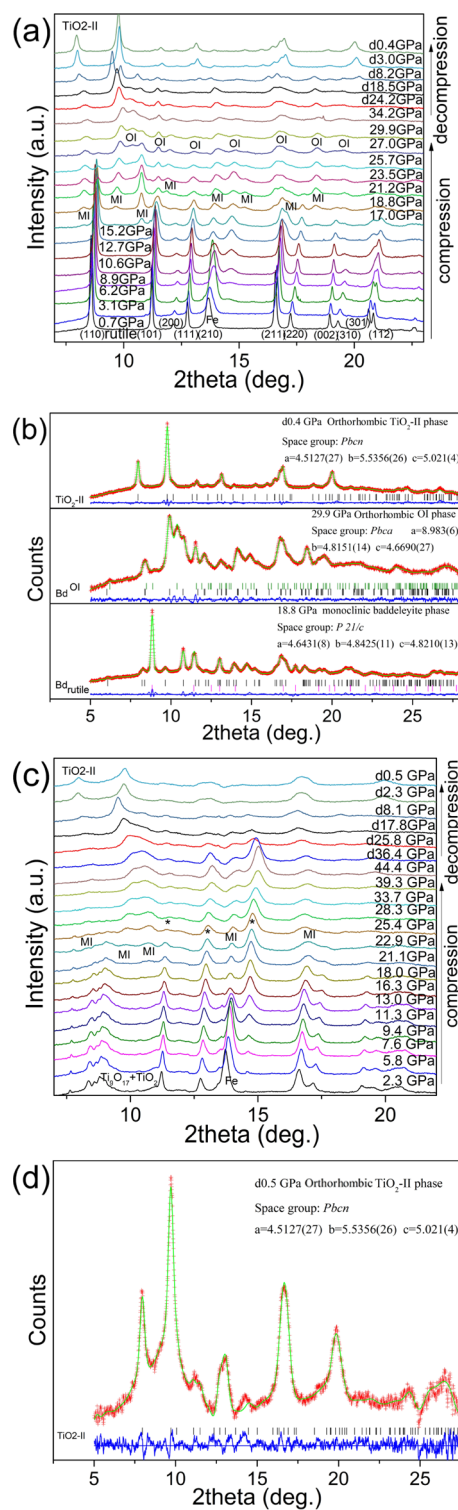


Figure 2. (a) High-pressure XRD patterns of TiO_2 hydrogenated at 500 °C and (b) example Rietveld fittings of the XRD data at 18.8 GPa (using a mixture of rutile and baddeleyite (“Bd” in the diagram)) and 29.9 GPa (using a mixture of TiO_2 -OI and baddeleyite) in compression and 0.4 GPa (using TiO_2 -II) in decompression. (c) High-pressure XRD patterns of TiO_2 hydrogenated at 800 °C and (d) a representative Rietveld fitting of the XRD data at 0.5 GPa (using TiO_2 -II) in decompression. Peaks marked as “Fe” were from the stainless steel gasket. Peaks marked by “*” are from an unidentified Ti_9O_{17} high-pressure phase.

above 20.3 GPa due to the large surface disorder in TiO₂ particles caused by the higher degree of reduction in hydrogenation. At ambient pressure after decompression, TiO₂-II was observed in the two samples (Figure S1b,d), consistent with the XRD data shown in Figure 2.

4.3. Electrical Transport Properties at High Pressure.

Figure S2 shows Nyquist plots⁵⁵ of one of the several ac impedance measurements on black titania hydrogenated at 500 °C. In a measurement, the relaxation processes in sample grain interiors (bulk) and grain boundaries cause the formation of two joint semicircles in the spectra (e.g., at 6.2 GPa, Figure S2b). The left semicircle (arc) in the low-frequency region represents the bulk conduction, and the right one in the high-frequency region corresponds to the grain boundary conduction.^{55–57}

The ac impedance spectra were modeled using an equivalent electrical circuit (inset in Figure S2a) describing the grain interior and grain boundary relaxation processes. By fitting the ac impedance spectra to the circuit model (using ZView software), circuit parameters were derived. Fitting results in Figure 3a show that the grain (bulk) resistance of the sample hydrogenated at 500 °C decreases markedly with increasing pressure below ~5 GPa. This is due to the initial formation of intimate contact between nanoparticles under compression. As pressure increases >5 GPa, the resistance increases slowly first at <~18 GPa, then there is a sharp increase at >~18 GPa, corresponding to the phase transition from rutile to baddeleyite. At >~32 GPa, the resistance tends to level off and then decreases, corresponding to the phase transition from baddeleyite to the TiO₂-OI phase. During decompression, the resistance decreases with decreasing pressure until ~5 GPa, below which the resistance increases with decreasing the pressure to the ambient value. This turning of the resistance at ~5 GPa corresponds to the phase transition from the mixture of TiO₂-OI and baddeleyite to the TiO₂-II phase.

The dc van der Pauw method⁵⁸ was used to measure the electrical resistivity of TiO₂ hydrogenated at 800 °C at high pressure. The basic equation is

$$\exp(-\pi R_1 d / \rho) + \exp(-\pi R_2 d / \rho) = 1 \quad (1)$$

where R_1 and R_2 are the two resistances measured by the two pairs of the probes in contact with the sample, $d = 28 \mu\text{m}$ is the thickness of the sample, and ρ is the sample resistivity in question.

Based on eq 1, the obtained pressure dependence of ρ of the sample is shown in Figure 3b. It is seen that the resistivity decreases dramatically with increasing pressure until <~3 GPa (Figure 3b inset) owing to the tightened contact of TiO₂ nanoparticles under compression. Upon further compression, the resistivity drop in the ~5–15 GPa range (Figure 3b) may be a result of the transition from the dominance of the resistivity by the initial particle compaction to that by the intrinsic carrier numbers controlled by the band gap of Ti₉O₁₇, as discussed below. On further compression >15 GPa, the resistivity increases steadily but more obviously after ~20 GPa. The faster increase in the resistivity at >~23 GPa can be attributed to the phase transition from rutile to baddeleyite as well as that from Ti₉O₁₇ to an unknown phase. In decompression, the resistivity continues to increase gradually till ~5 GPa where an abrupt increase is observed, corresponding to the conversion of the baddeleyite phase to the TiO₂-II phase. The gradual increase of the resistivity in decompression is possibly related to the gradual oxidation and

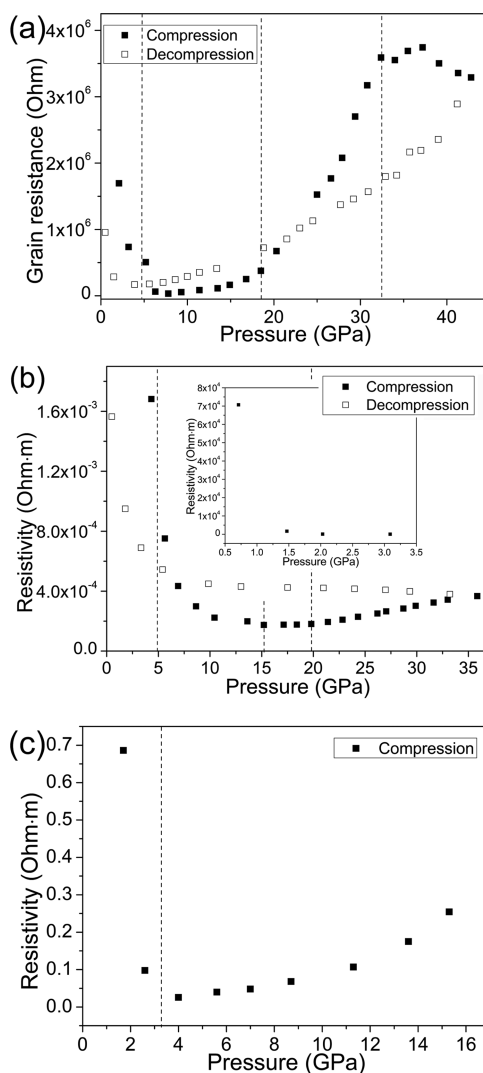


Figure 3. Pressure dependence of the grain resistance of TiO₂ particles hydrogenated at 500 °C measured from ac impedance spectroscopy (a) and that of the electrical resistivity of TiO₂ particles hydrogenated at 800 °C (b) and 500 °C (c) measured using the Van der Pauw method. The inset in (b) shows the very high electrical resistivity in compression below ~3 GPa. Vertical dashed lines indicate onsets of apparent resistance/resistivity changes.

conversion of Ti₉O₁₇ to the baddeleyite phase, as inferred from the XRD data which show that in decompression no Ti₉O₁₇ diffraction peaks were observed (Figure 2c). As the content of Ti₉O₁₇ (that has a narrow band gap) reduces gradually in decompression, the content of baddeleyite (that has a wide band gap) increases, which leads to the increase of the resistance during decompression (see below).

To directly compare the electrical conductivities of the two samples hydrogenated at 500 and 800 °C, we also acquired the resistivity of TiO₂ hydrogenated at 500 °C (below 16 GPa) using the van der Pauw method (Figure 3c). Comparing Figure 3b with Figure 3c, one sees that the resistivity of TiO₂ hydrogenated at 800 °C is about 2–3 orders of magnitude lower than that of TiO₂ hydrogenated at 500 °C at the same pressure after initial particle compaction (>~5 GPa), revealing a significant enhancement in electrical transport as a result of much higher degree of hydrogenation.

4.4. Mechanism for Pressure Dependence of the Electrical Conductivity of Black Titania. The electrical conductivity of a material should be scaled with the carrier concentration and carrier mobility, as demonstrated by previous studies.^{59,60} For semiconductors, the carrier concentration is closely related to the band gap. Thus, we hypothesize that the pressure dependence of the HP electrical resistance of black titania is governed by the variation of the carrier concentration with the pressure, which is again determined by the pressure dependence of the band gap.

The carrier concentration in a semiconductor is the number of free electrons (or holes) per unit volume distributed in the conduction band (or the valence band). For an intrinsic semiconductor, the electron and hole concentrations are equal in magnitude and are proportional to $\exp(-E_g/(2kT))$,⁶¹ where E_g is the band gap, T is the absolute temperature, and k is the Boltzmann constant ($1.381 \times 10^{-23} \text{ J K}^{-1}$). Thus, the grain resistance of black titania is proportional to $\exp(E_g/(2kT))$. As a result, the larger the band gap, the higher the electrical resistance (resistivity). We now examine this deduction using both the UV-vis data and the DFT calculations (below).

Tauc-Mott plots⁶² of the UV-vis absorption data were used to derive the band gaps of the TiO_2 samples in the range of ~ 0 –15 GPa (see Figure S3), as depicted in Figure 4).

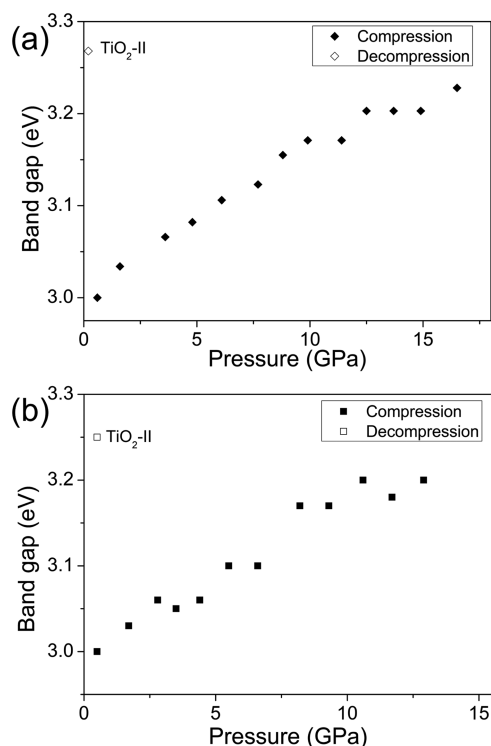


Figure 4. Pressure dependence of the band gaps of TiO_2 hydrogenated at 500 °C (a) and 800 °C (b).

Figure 4a describes the pressure dependence of the band gap of rutile in black titania hydrogenated at 500 °C, whereas Figure 4b, the pressure dependence of the apparent band gap of the mixture of rutile and Ti_9O_{17} in the sample hydrogenated at 800 °C. Figure 4a shows that the band gap of rutile increases with increasing pressure, which correlates well with the pressure dependence of the measured resistance in the range of ~ 5 –15 GPa shown in Figure 3a (initial particle compaction

stage at < 5 GPa is excluded). This supports our above deduction that the larger the band gap, the higher the electrical resistance. In Figure 3b, the resistivity at < 15 GPa shows continuous dropping possibly because of continued particle compaction, which cannot be directly related to the pressure dependence of the band gap shown in Figure 4b.

For a complete compression–decompression cycle, to correlate the electrical resistance (resistivity) with the band gap of TiO_2 at different pressures (Figure 3), pressure-dependent band gaps of the phases present are needed. These are not all available from experiments (except for rutile at $< \sim 15$ GPa shown in Figure 4). Thus, we used DFT to calculate the band gaps of TiO_2 and Ti_9O_{17} phases that may involve in the phase transitions. First, the crystal structures of concerned Ti–O phases at chosen pressures were optimized, and the obtained lattice parameters are listed in Tables S1 and S2. It is seen that the optimized values are close to the available literature data. Then, the densities of states (DOSs) were calculated and are summarized in Figures S4 and S5 from which the pressure-dependent band gaps of various TiO_2 phases and Ti_9O_{17} are obtained, as shown in Figure 5.

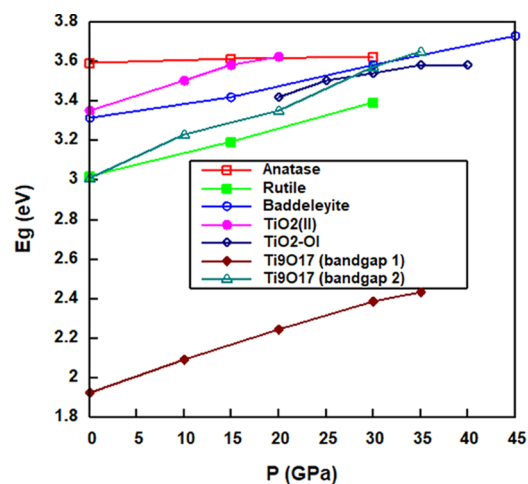


Figure 5. Calculated band gaps of several TiO_2 phases and the triclinic Ti_9O_{17} phase at different pressures. Ti_9O_{17} has two band gaps (see Figure S5).

Figure 5 shows that for a given Ti–O phase, the higher the pressure, the larger the band gap (in approximate linearity). The calculated band gap of rutile in the range of 0–15 GPa agrees quite well with that obtained from the UV-vis experiment (see Figure 4a). Using Figure 5, we can interpret the observed variation of the electrical resistance with the pressure (Figure 3a) following an “ E_g route” shown in Figure S6a. In compression, after initial particle compaction at ~ 5 GPa, the resistance increases gradually with the pressure up to ~ 18 GPa (Figure 3a), corresponding to the band gap widening of rutile (Figure S6a). From ~ 18 to 33 GPa, the resistance increases dramatically (Figure 3a) owing to the transition of rutile to the baddeleyite phase, which has a band gap of ~ 0.2 eV higher than that of rutile (Figure S6a). At above ~ 33 GPa, the baddeleyite phase starts to form the $\text{TiO}_2\text{-OI}$ phase, which has a lower band gap than that of baddeleyite (Figure S6a), causing the resistance to decrease (Figure 3a). In decompression, the OI phase gradually transforms back to the baddeleyite phase and hence the band gap (Figure S6a) and the resistance (Figure 3a) decrease until ~ 3 GPa, at which the

baddeleyite phase transforms to the TiO_2 -II phase. As TiO_2 -II has a higher band gap than baddeleyite (Figure S6a), the resistance increases again at <3 GPa (Figure 3a). The calculated band gap of TiO_2 -II at ambient pressure (~ 3.35 eV; Figure S6a) is comparable to the value obtained from the UV-vis absorption experiment (3.27 eV; Figure 4b). The good correlation between the “ E_g route” (Figure S6a) and the pressure dependence of the resistance (Figure 3a) once again supports our above deduction. We note, however, that there are some differences between the phase transition pressures estimated from the electrical transport measurements (e.g., ~ 33 GPa from baddeleyite to the OI phase) and those by HP-XRD (e.g., ~ 27 GPa from baddeleyite to the OI phase). These may arise from the difference in the hydrostatic conditions, as no pressure medium was used in the HP-resistance measurements, whereas the methanol-ethanol mixture was used in the HP-XRD.

A similar “ E_g route” scheme (Figure S6b) can be used to explain the observed pressure dependence of the resistivity of black titania hydrogenated at 800 °C (Figure 3b). From the DFT calculations, it was found that the Magneli phase Ti_9O_{17} has a mid-band (minor conduction band) between the valence band and the major conduction band (Figure S5), leading to two band gaps with E_{g1} being ~ 1.9 eV and E_{g2} ~ 3.0 eV at 0 GPa (Figure 5). The existence of the first band gap facilitates light absorption in the visible light range, as confirmed by the UV-vis absorption of the 800 °C sample shown in Figure 1d, which enhances the electrical conductivity. Thus, the resistivity of this sample with mixed phases should be governed by the first band gap of Ti_9O_{17} rather than by that of rutile. When this sample is compressed (after the initial particle compaction in the 0 to ~ 15 GPa range; see above), the resistivity increases gradually (Figure 3b) following the trend of the pressure dependence of E_{g1} of Ti_9O_{17} , and this trend continues even after its transition to an unknown HP phase (Figure S6b). Upon decompression, the unknown HP phase is converted gradually to the baddeleyite phase after oxidation (see above), making the apparent band gap increase continuously and then suddenly at ~ 5 GPa due to a full transition of the baddeleyite phase to TiO_2 -II (Figure S6b). Thus, in accordance with the apparent band gap change in decompression, the resistivity increases first gradually and then rapidly near the ambient condition (Figure 3b).

In view of above discussions, we conclude that the pressure dependence of the electrical conductivity of black titania is determined by the pressure tuning of the number of free electrons (or holes) distributed in the conduction (or valence) band via the change of the band gap and crystal structure with the pressure while in compression.

5. CONCLUSIONS

In this work, we prepared black titania samples through reduction of rutile by hydrogen at temperatures from 500 to 800 °C. Then, using synchrotron high-pressure XRD, Raman, and UV-vis spectroscopy as well as electrical transport measurements, we studied the pressure effects on the structures, the electrical conductivity, and light absorption of two of the hydrogenated TiO_2 samples. Electron density of states and band gaps of involved Ti-O phases were calculated using DFT methods for elucidating the relationship between the observed electrical conductivity and crystal structure at high pressure. It is found that in compression of TiO_2 reduced by H_2 at 500 °C, there is a phase transition from rutile to

baddeleyite at ~ 17.0 GPa, which then transforms to TiO_2 -OI at ~ 27.0 GPa; in decompression, TiO_2 -OI transforms to TiO_2 -II at ~ 3 GPa. In contrast, in compression of TiO_2 reduced by H_2 at 800 °C consisting of a rutile and a Magneli phase Ti_9O_{17} initially, a phase transition from rutile to baddeleyite at ~ 21.0 GPa and a transition of the Magneli phase to an unknown phase were observed. The observed complex variation of the electrical resistance (resistivity) of black titania with pressure is attributed to the change in the carrier concentrations due to the changes of the band gaps of involved Ti-O phases under compression. For a specific phase, the higher the pressure, the larger the band gap and hence the higher the electrical resistivity. Comparing the two samples, we found that there is a significant enhancement in electrical transport in TiO_2 hydrogenated at 800 °C in comparison to that in the one hydrogenated at 500 °C at high pressures due to the higher degree of hydrogenation that led to the formation of Ti_9O_{17} . This study unveils the mechanism dictating the pressure dependence of the electrical conductivity of black titania. It will have important implications for development of new applications of hydrogenated TiO_2 aside from photocatalysis, such as for use as conjugated pressure and light sensors.

■ ASSOCIATED CONTENT

Supporting Information

The Supporting Information is available free of charge on the ACS Publications website at DOI: 10.1021/acs.jpcc.8b12056.

High-pressure Raman spectroscopy data, pressure dependence of ac impedance spectra, Tauc-Mott plots of UV-vis absorption spectra, DFT-calculated DOS and optimized unit cell parameters of TiO_2 and Ti_9O_{17} phases at different pressures (PDF)

■ AUTHOR INFORMATION

Corresponding Author

*E-mail: hengzhong.zhang@hpstar.ac.cn. Phone: +86-21-80177095.

ORCID

Qiwu Shi: 0000-0002-4776-5727

Zhongwu Wang: 0000-0001-9742-5213

Hengzhong Zhang: 0000-0003-2322-2274

Notes

The authors declare no competing financial interest.

■ ACKNOWLEDGMENTS

The high-pressure synchrotron X-ray diffraction was conducted at the high energy beamline station B1 of Cornell High Energy Synchrotron Source, New York. Part of the computations was conducted using the Tianhe-2 supercomputer of the National Supercomputer Center in Guangzhou, China. Q.S. thanks the financial support by the Chinese NSAF Grant No. U1730138.

■ REFERENCES

- (1) Linsebigler, A. L.; Lu, G.; Yates, J. T., Jr. Photocatalysis on TiO_2 Surfaces: Principles, Mechanisms, and Selected Results. *Chem. Rev.* **1995**, *95*, 735–758.
- (2) Fujishima, A.; Zhang, X.; Tryk, D. A. TiO_2 Photocatalysis and Related Surface Phenomena. *Surf. Sci. Rep.* **2008**, *63*, 515–582.
- (3) Zheng, Q.; Zhou, B.; Bai, J.; Li, L.; Jin, Z.; Zhang, J.; Li, J.; Liu, Y.; Cai, W.; Zhu, X. Self-Organized TiO_2 Nanotube Array Sensor for

the Determination of Chemical Oxygen Demand. *Adv. Mater.* **2008**, *20*, 1044–1049.

(4) Crossland, E. J.; Noel, N.; Sivaram, V.; Leijtens, T.; Alexander-Webber, J. A.; Snaith, H. J. Mesoporous TiO₂ Single Crystals Delivering Enhanced Mobility and Optoelectronic Device Performance. *Nature* **2013**, *495*, 215.

(5) Gu, J.; Yan, Y.; Young, J. L.; Steirer, K. X.; Neale, N. R.; Turner, J. A. Water Reduction by a p-GaInP₂ Photoelectrode Stabilized by an Amorphous TiO₂ Coating and a Molecular Cobalt Catalyst. *Nat. Mater.* **2016**, *15*, 456.

(6) Yang, C.; Wang, Z.; Lin, T.; Yin, H.; Lü, X.; Wan, D.; Xu, T.; Zheng, C.; Lin, J.; Huang, F.; et al. Core-Shell Nanostructured “Black” Rutile Titania as Excellent Catalyst for Hydrogen Production Enhanced by Sulfur Doping. *J. Am. Chem. Soc.* **2013**, *135*, 17831–17838.

(7) Liu, L.; Chen, X. Titanium Dioxide Nanomaterials: Self-Structural Modifications. *Chem. Rev.* **2014**, *114*, 9890–9918.

(8) Asahi, R.; Morikawa, T.; Ohwaki, T.; Aoki, K.; Taga, Y. Visible-Light Photocatalysis in Nitrogen-Doped Titanium Oxides. *Science* **2001**, *293*, 269–271.

(9) Inturi, S. N. R.; Boningari, T.; Suidan, M.; Smirniotis, P. G. Flame Aerosol Synthesized Cr Incorporated TiO₂ for Visible Light Photodegradation of Gas Phase Acetonitrile. *J. Phys. Chem. C* **2014**, *118*, 231–242.

(10) Choi, W.; Termin, A.; Hoffmann, M. R. Effects of Metal-Ion Dopants on the Photocatalytic Reactivity of Quantum-Sized TiO₂ Particles. *Angew. Chem., Int. Ed.* **1994**, *33*, 1091–1092.

(11) Liu, G.; Han, C.; Pelaez, M.; Zhu, D.; Liao, S.; Likodimos, V.; Kontos, A. G.; Falaras, P.; Dionysiou, D. D. Enhanced Visible Light Photocatalytic Activity of C–N-Codoped TiO₂ Films for the Degradation of Microcystin-LR. *J. Mol. Catal. A: Chem.* **2013**, *372*, 58–65.

(12) Wu, X.; Yin, S.; Dong, Q.; Guo, C.; Kimura, T.; Matsushita, J. I.; Sato, T. Photocatalytic Properties of Nd and C Codoped TiO₂ with the Whole Range of Visible Light Absorption. *J. Phys. Chem. C* **2013**, *117*, 8345–8352.

(13) Chen, X.; Liu, L.; Peter, Y. Y.; Mao, S. S. Increasing Solar Absorption for Photocatalysis with Black Hydrogenated Titanium Dioxide Nanocrystals. *Science* **2011**, *331*, 746–750.

(14) Lü, X.; Chen, A.; Luo, Y.; Lu, P.; Dai, Y.; Enriquez, E.; Dowden, P.; Xu, H.; Kotula, P. G.; Azad, A. K.; Yarotski, D. A.; Prasankumar, R. P.; Taylor, A. J.; Thompson, J. D.; Jia, Q. Conducting Interface in Oxide Homo Junction: Understanding of Superior Properties in Black TiO₂. *Nano Lett.* **2016**, *16*, 5751–5755.

(15) Liu, L.; Peter, Y. Y.; Chen, X.; Mao, S. S.; Shen, D. Z. Hydrogenation and Disorder in Engineered Black TiO₂. *Phys. Rev. Lett.* **2013**, *111*, No. 065505.

(16) Naldoni, A.; Allietti, M.; Santangelo, S.; Marelli, M.; Fabbri, F.; Cappelli, S.; Bianchi, C. L.; Psaro, R.; Dal Santo, V. Effect of Nature and Location of Defects on Bandgap Narrowing in Black TiO₂ Nanoparticles. *J. Am. Chem. Soc.* **2012**, *134*, 7600–7603.

(17) Chen, X.; Liu, L.; Huang, F. Black Titanium Dioxide (TiO₂) Nanomaterials. *Chem. Soc. Rev.* **2015**, *44*, 1861–1885.

(18) Selcuk, S.; Selloni, A. Facet-Dependent Trapping and Dynamics of Excess Electrons at Anatase TiO₂ Surfaces and Aqueous Interfaces. *Nat. Mater.* **2016**, *15*, 1107.

(19) Zhang, H.; Banfield, J. F. Structural Characteristics and Mechanical and Thermodynamic Properties of Nanocrystalline TiO₂. *Chem. Rev.* **2014**, *114*, 9613–9644.

(20) Hwang, S. L.; Shen, P.; Chu, H. T.; Yui, T. F. Nanometer-Size α -PbO₂-Type TiO₂ in Garnet: A Thermobarometer for Ultrahigh-Pressure Metamorphism. *Science* **2000**, *288*, 321–324.

(21) Dewhurst, J. K.; Lowther, J. E. High-Pressure Structural Phases of Titanium Dioxide. *Phys. Rev. B* **1996**, *54*, No. R3673.

(22) Matsui, M.; Akaogi, M. Molecular Dynamics Simulation of the Structural and Physical Properties of the Four Polymorphs of TiO₂. *Mol. Simul.* **1991**, *6*, 239–244.

(23) Gerward, L.; Staun Olsen, J. Post-Rutile High-Pressure Phases in TiO₂. *J. Appl. Crystallogr.* **1997**, *30*, 259–264.

(24) Sasaki, T. Stability of Rutile-Type TiO₂ under High Pressure. *J. Phys.: Condens. Matter* **2002**, *14*, 10557.

(25) Olsen, J. S.; Gerward, L.; Jiang, J. Z. On the Rutile/ α -PbO₂-Type Phase Boundary of TiO₂. *J. Phys. Chem. Solids* **1999**, *60*, 229–233.

(26) Wang, Z.; Saxena, S. K.; Pischedda, V.; Liermann, H. P.; Zha, C. S. X-Ray Diffraction Study on Pressure-Induced Phase Transformations in Nanocrystalline Anatase/Rutile (TiO₂). *J. Phys.: Condens. Matter* **2001**, *13*, 8317.

(27) Bian, K.; Richards, B. T.; Yang, H.; Bassett, W.; Wise, F. W.; Wang, Z.; Hanrath, T. Optical Properties of PbS Nanocrystal Quantum Dots at Ambient and Elevated Pressure. *Phys. Chem. Chem. Phys.* **2014**, *16*, 8515–8520.

(28) Hammersley, A. P.; Svensson, S. O.; Hanfland, M.; Fitch, A. N.; Häussermann, D. Two-Dimensional Detector Software: From Real Detector to Idealised Image or Two-Theta Scan. *High Pressure Res.* **1996**, *14*, 235–248.

(29) Toby, B. H. Expgui, a Graphical User Interface for GSAS. *J. Appl. Crystallogr.* **2001**, *34*, 210–213.

(30) Ramadan, A. A.; Gould, R. D.; Ashour, A. On the Van Der Pauw Method of Resistivity Measurements. *Thin Solid Films* **1994**, *239*, 272–275.

(31) Giannozzi, P.; Andreussi, O.; Brumme, T.; Bunau, O.; Nardelli, M. B.; Calandra, M.; Car, R.; Cavazzoni, C.; Ceresoli, D.; Cococcioni, M.; et al. Advanced Capabilities for Materials Modelling with Quantum ESPRESSO. *J. Phys.: Condens. Matter* **2017**, *29*, No. 465901.

(32) Nishihara, S. Burai 1.3, A GUI of Quantum ESPRESSO. <http://nishihara.wixsite.com/burai>.

(33) Blöchl, P. E. Projector Augmented-Wave Method. *Phys. Rev. B* **1994**, *50*, No. 17953.

(34) Perdew, J. P.; Burke, K.; Ernzerhof, M. Generalized Gradient Approximation Made Simple. *Phys. Rev. Lett.* **1996**, *77*, 3865.

(35) Anisimov, V. I.; Zaanen, J.; Andersen, O. K. Band theory and Mott insulators: Hubbard *U* instead of Stoner *I*. *Phys. Rev. B* **1991**, *44*, No. 943.

(36) Arroyo-de Dompablo, M. E.; Morales-García, A.; Taravillo, M. DFT + *U* Calculations of Crystal Lattice, Electronic Structure, and Phase Stability under Pressure of TiO₂ Polymorphs. *J. Chem. Phys.* **2011**, *135*, No. 054503.

(37) Shin, J. Y.; Joo, J. H.; Samuelis, D.; Maier, J. Oxygen-Deficient TiO_{2- δ} Nanoparticles Via Hydrogen Reduction for High Rate Capability Lithium Batteries. *Chem. Mater.* **2012**, *24*, 543–551.

(38) Qiu, J.; Li, S.; Gray, E.; Liu, H.; Gu, Q. F.; Sun, C.; Lai, C.; Zhao, H.; Zhang, S. Hydrogenation Synthesis of Blue TiO₂ for High-Performance Lithium-Ion Batteries. *J. Phys. Chem. C* **2014**, *118*, 8824–8830.

(39) Sekiya, T.; Yagisawa, T.; Kamiya, N.; Das Mulmi, D.; Kurita, S.; Murakami, Y.; Kodaira, T. Defects in Anatase TiO₂ Single Crystal Controlled by Heat Treatments. *J. Phys. Soc. Jpn.* **2004**, *73*, 703–710.

(40) Hellenbrandt, M. The Inorganic Crystal Structure Database (ICSD)—Present and Future. *Crystallogr. Rev.* **2004**, *10*, 17–22.

(41) Harada, S.; Tanaka, K.; Inui, H. Thermoelectric Properties and Crystallographic Shear Structures in Titanium Oxides of the Magnéli Phases. *J. Appl. Phys.* **2010**, *108*, No. 083703.

(42) Andersson, S.; Collén, B.; Kuylenstierna, U.; Magnéli, A. Phase Analysis Studies on the Titanium-Oxygen System. *Acta Chem. Scand.* **1957**, *11*, 1641–1652.

(43) Liborio, L.; Harrison, N. Thermodynamics of Oxygen Defective Magnéli Phases in Rutile: A First-Principles Study. *Phys. Rev. B* **2008**, *77*, No. 104104.

(44) Desgreniers, S.; Lagarec, K. High-Density ZrO₂ and HfO₂: Crystalline Structures and Equations of State. *Phys. Rev. B* **1999**, *59*, No. 8467.

(45) Adams, D. M.; Leonard, S.; Russell, D. R.; Cernik, R. J. X-Ray Diffraction Study of Hafnia under High Pressure Using Synchrotron Radiation. *J. Phys. Chem. Solids* **1991**, *52*, 1181–1186.

- (46) Leger, J. M.; Tomaszewski, P.; Atouf, A.; Pereira, A. S. Pressure-Induced Structural Phase Transitions in Zirconia under High Pressure. *Phys. Rev. B* **1993**, *47*, No. 14075.
- (47) Leger, J. M.; Atouf, A.; Tomaszewski, P.; Pereira, A. S. Pressure-Induced Phase Transitions and Volume Changes in HfO₂ up to 50 GPa. *Phys. Rev. B* **1993**, *48*, No. 93.
- (48) Dubrovinsky, L. S.; Dubrovinskaia, N. A.; Swamy, V.; Muscat, J.; Harrison, N. M.; Ahuja, R.; Holm, B.; Johansson, B. Materials Science: The Hardest Known Oxide. *Nature* **2001**, *410*, 653.
- (49) Haines, J.; Leger, J. M.; Schulte, O. The High-Pressure Phase Transition Sequence from the Rutile-Type through to the Cotunnite-Type Structure In. *J. Phys.: Condens. Matter* **1996**, *8*, 1631.
- (50) Lowther, J. E.; Dewhurst, J. K.; Leger, J. M.; Haines, J. Relative Stability of ZrO₂ and HfO₂ Structural Phases. *Phys. Rev. B* **1999**, *60*, No. 14485.
- (51) Dubrovinskaia, N. A.; Dubrovinsky, L. S.; Ahuja, R.; Prokopenko, V. B.; Dmitriev, V.; Weber, H. P.; Osorio-Guillen, J.; Johansson, B. Experimental and Theoretical Identification of a New High-Pressure TiO₂ Polymorph. *Phys. Rev. Lett.* **2001**, *87*, No. 275501.
- (52) Haines, J.; Leger, J. M. X-Ray Diffraction Study of TiO₂ up to 49 GPa. *Phys. B: Condens. Matter* **1993**, *192*, 233–237.
- (53) Sato, H.; Endo, S.; Sugiyama, M.; Kikegawa, T.; Shimomura, O.; Kusaba, K. Baddeleyite-Type High-Pressure Phase of TiO₂. *Science* **1991**, *251*, 786–788.
- (54) Mei, Z. G.; Wang, Y.; Shang, S.; Liu, Z. K. First-Principles Study of the Mechanical Properties and Phase Stability of TiO₂. *Comput. Mater. Sci.* **2014**, *83*, 114–119.
- (55) Abrantes, J. C.; Labrincha, J. A.; Frade, J. R. An Alternative Representation of Impedance Spectra of Ceramics. *Mater. Res. Bull.* **2000**, *35*, 727–740.
- (56) Li, Y.; Gao, Y.; Han, Y.; Wang, Q.; Li, Y.; Su, N.; Zhang, J.; Liu, C.; Ma, Y.; Gao, C. High-Pressure Electrical Transport Behavior in WO₃. *J. Phys. Chem. C* **2012**, *116*, 5209–5214.
- (57) He, C.; Gao, C.; Ma, Y.; Li, M.; Hao, A.; Huang, X.; Liu, B.; Zhang, D.; Yu, C.; Zou, G.; et al. In Situ Electrical Impedance Spectroscopy under High Pressure on Diamond Anvil Cell. *Appl. Phys. Lett.* **2007**, *91*, No. 092124.
- (58) van der Pauw, L. J. A. Method of Measuring Specific Resistivity and Hall Effect of Discs of Arbitrary Shape. *Philips Res. Rep.* **1958**, *13*, 1–9.
- (59) Ke, F.; Yang, J.; Liu, C.; Wang, Q.; Li, Y.; Zhang, J.; Wu, L.; Zhang, X.; Han, Y.; Wu, B. High-Pressure Electrical-Transport Properties of SnS: Experimental and Theoretical Approaches. *J. Phys. Chem. C* **2013**, *117*, 6033–6038.
- (60) Li, Y.; Wang, Y.; Tang, R.; Wang, X.; Zhu, P.; Zhao, X.; Gao, C. Structural Phase Transition and Electrical Transport Properties of CuInS₂ Nanocrystals under High Pressure. *J. Phys. Chem. C* **2015**, *119*, 2963–2968.
- (61) Hu, C. *Modern Semiconductor Devices for Integrated Circuits*; Prentice Hall: Upper Saddle River, NJ, 2010; Vol. 1.
- (62) Chernyshova, I. V.; Ponnurangam, S.; Somasundaran, P. On the Origin of an Unusual Dependence of (bio)Chemical Reactivity of Ferric Hydroxides on Nanoparticle Size. *Phys. Chem. Chem. Phys.* **2010**, *12*, 14045–14056.